RSC Advances

ROYAL SOCIETY OF CHEMISTRY

www.rsc.org/advances

Near-infrared luminescence and SMM behaviors of a family of dinuclear lanthanide 8-quinolinolate complexes

Hai-Yun Shen, Wen-Min Wang, Hong-Ling Gao, Jian-Zhong Cui *

Abstract

A new family of lanthanide complexes, $[Ln_2(dbm)_4(OQ)_2(CH_3OH)_2]$ (Ln = Nd (**1**), Tb (**2**), Dy (**3**), Ho (**4**); dbm = dibenzoylmethanate, OQ = 8-quinolinolate), and $[Er_2(dbm)_4(OQ)_2(CH_3OH)]\cdot CH_3COCH_3$ (**5**) were synthesized and characterized using single-crystal X-ray diffraction, elemental analysis (EA), thermal gravimetric analysis (TGA), powder X-ray diffraction (PXRD) and UV-vis spectra. X-ray crystallographic analyses reveal that **1**–**5** are μ-phenol bridged dinuclear complexes. For complexes **1**−**4**, each Ln^{III} ion is eight-coordinated with two bidentate dbm and two μ-phenol bridging OQ ligands and one methanol molecule. Complex **1** in the solid-state displays typical emissions of the Nd^{III} ions in the NIR region. Magnetic measurements were carried out on complexes **1**–**5**. Dynamic magnetic studies reveal single-molecule magnet (SMM) behavior for complex **3.** Fitting the dynamic magnetic data to the Arrhenius law gives an energy barrier $\Delta E/k_B$ = 109.5 K and pre-exponential factor $\tau_0 = 4.23\times10^{-9}$ s under 3000Oe dc field.

Introduction

Single-molecule magnets (SMMs) continue to receive much interest due to their huge potential applications in many fields such as high-density information storage,[1] quantum computing,[2] molecule-based spintronics devices.[3] As is now reasonably well understood, SMM behavior is of molecular origin and can be observed in molecules which possess

Department of Chemistry, Tianjin University, Tianjin 300072, P. R. China.
E-mail: cuijianzhong@tju.edu.cn
Electronic supplementary information (ESI) available: Supplementary Experimental Section. Tables of selected bond lengths and angles. Fig. S1 to S7. CCDC: 1448498-1448502(**1**−**5**).

a large-spin ground state along with an intrinsic magnetic anisotropy.[4] The general approach to creating new SMMs is to enhance negative Ising (or easy-axis) types of magneto anisotropy (*D*) and large ground spin states in the system.[5] Since Ishikawa and co-workers reported the first Ln-ion-based SMMs $(Bu_4N)[Tb(Pc)_2]$ (H_2Pc = phthalocyanine),[6] more and more attentions have been paid to lanthanide complexes in the pursuit of SMMs with higher anisotropic barriers, because of their highly anisotropic nature arising from large unquenched orbital angular momentum.[7] Constructing Ln-based SMMs, the Dy^{III} ion has long occupied a vital position to obtaining higher effective energy barriers because of its large magnetic anisotropy originating from the $^6H_{15/2}$ state.[8] Up to now, a large quantity of Dy^{III}-containing SMMs varying from mononuclear to dodecanuclear, and even up to tetracosanuclear, have been discovered.[9] However, the study and control of the magnetic properties in such strongly anisotropic systems still poses a challenge because of the complicated electronic structures of lanthanide ions and the great complexity of anisotropy properties for a cluster.[10] With this in mind, lower-nuclearity lanthanide clusters seem to be of great interest because of the relative simplification in the modulation of the relaxation dynamics. Dinuclear dysprosium (Dy_2) systems have long occupied a vital position in displaying large thermal energy barrier and investigating the magnetic relaxation behavior.

Among organic ligands, 8-hydroxyquinoline (HOQ) and its derivatives attract notable attention for constructing luminescent complexes;[11] for example, tris-8-(hydroxyquinoline) aluminum has been developed as an efficient electroluminescence material in organic light emitting diode (OLED) fabrication.[12] Moreover, thanks to its low energy triplet state (17100 cm^{-1}, 585nm), 8-hydroxyquinoline is suitable for sensitizing the NIR emission of lanthanide ions.[13]

Recently our group have previously synthesized a series of typical phenoxo-O-bridged lanthanide(III) dinuclear complexes by using 8-hydroxyquinoline derivatives and different

β-diketonate coligands.[14] It demonstrates that the replacement of *β*-diketonate ligand can influence the SMM behaviors. In order to make further investigation on how the ligand field perturbation affects the structures of Ln^{III} complexes and their magnetic relaxation behaviors in dinuclear dysprosium (Dy_2) clusters. Herein, five dinuclear lanthanide complexes $[Ln_2(dbm)_4(OQ)_2(CH_3OH)_2]$ (Ln = Nd (**1**), Tb (**2**), Dy (**3**), Ho (**4**)) and $[Er_2(dbm)_4(OQ)_2(CH_3OH)]\cdot CH_3COCH_3$ (**5**) were successfully synthesized by 8-hydroxyquinoline and dibenzoylmethanate (dbm) ligands. Magnetic measurements on complexes **1**–**5** were carried out. Magnetic studies reveal single-molecule magnet (SMM) behavior for complex **3**; meanwhile, complex **2** displays no SMM behavior.

Experimental section

Materials and general methods.

All chemicals and solvents were commercially available and used without further purification. Elemental analyses for C, H and N were performed on a PerkinElmer 240 CHN elemental analyzer. IR spectra were recorded in the range of 400−4000 cm^{-1} with a Bruker TENOR 27 spectrophotometer using a KBr pellet. UV-vis spectra were recorded on a UV-3600 UV-VIS-NIR spectrophotometer at room temperature. Thermogravimetric analysis (TGA) experiments were obtained using a NETZSCHTG 209 thermal analyzer in a static atmosphere with a sample size and a heating rate of 10 °C min^{-1}. Powder X-ray diffraction (PXRD) measurements were collected on a Rigaku D/max 2500/pc/X-ray powder diffractometer with Cu-*Kα* radiation (λ = 1.540598 Å). NIR spectra were measured on a Horiba Jobin Yvon Fluorolog-3-tau fluorescence spectrophotometer, equipped with a 450 W Xe lamp as the excitation source and a liquid-nitrogen-cooled InGaAs as detector. Magnetic measurements were performed using an MPMS XL-7 SQUID magnetometer.

Preparation of complexes $[Ln_2(dbm)_4(OQ)_2(CH_3OH)_2]$ (Ln = Nd (1), Tb (2), Dy (3), Ho (4)) and $[Er_2(dbm)_4(OQ)_2(CH_3OH)]\cdot CH_3COCH_3$(5).

All five of the complexes were

synthesized by the same method. $Ln(dbm)_2 \cdot 2H_2O$ (0.025 mmol) was dissolved in 10 mL of acetone. A 10 mL CH_3OH solution of HOQ (0.025 mmol) was added. The resulting solution was stirred for 4 h at room temperature. After being filtered, the filtrate was concentrated by slow evaporation at 4 °C. After a few days, yellow crystals suitable for single-crystal X-ray analysis were obtained.

[**$Nd_2(dbm)_4(OQ)_2(CH_3OH)_2$**] (**1**). Yield: 60% based on Nd. Anal. Calcd (%) for $[Nd_2(dbm)_4(OQ)_2(CH_3OH)_2]$ (fw = 1533.81): C, 62.65; H, 4.21; N, 1.83; Found: C, 62.60; H, 4.19; N, 1.80%. IR (cm^{-1}): 3058w, 1597s, 1550s, 1518s, 1478s, 1397s, 1312m, 1221w, 1102m, 1024w, 786w, 725w, 689w, 609w.

[$Tb_2(dbm)_4(OQ)_2(CH_3OH)_2$] (**2**). Yield: 55% based on Tb. Anal. Calcd (%) for $[Tb_2(dbm)_4(OQ)_2(CH_3OH)_2]$ (fw = 1563.17): C, 61.46; H, 4.13; N, 1.79; Found: C, 61.40; H, 4.10; N, 1.74%. IR (cm^{-1}): 3058w, 1597s, 1551s, 1519s, 1478s, 1401s, 1313m, 1222w, 1103m, 1024w, 786w, 725w, 689w, 610w.

[**$Dy_2(dbm)_4(OQ)_2(CH_3OH)_2$**] (**3**). Yield: 58% based on Dy. Anal. Calcd (%) for $[Dy_2(dbm)_4(OQ)_2(CH_3OH)_2]$ (fw = 1570.34): C, 61.19; H, 4.11; N, 1.78; Found: C, 61.11; H, 4.07; N, 1.72%. IR (cm^{-1}): 3058w, 1597s, 1552s, 1519s, 1478s, 1402s, 1314m, 1222w, 1103m, 1024w, 785w, 727w, 689w, 610w.

[**$Ho_2(dbm)_4(OQ)_2(CH_3OH)_2$**] (**4**). Yield: 55% based on Ho. Anal. Calcd (%) for $[Ho_2(dbm)_4(OQ)_2(CH_3OH)_2]$ (fw = 1575.2): C, 60.99; H, 4.10; N, 1.78; Found: C, 60.92; H, 4.05; N, 1.72%. IR (cm^{-1}): 3058w, 1597s, 1552s, 1518s, 1478s, 1400s, 1312m, 1222w, 1103m, 1024w, 786w, 725w, 689w, 609w.

[**$Er_2(dbm)_4(OQ)_2(CH_3OH)$**]·**$CH_3COCH_3$** (**5**). Yield: 58% based on Er. Anal. Calcd (%) for $[Er_2(dbm)_4(OQ)_2(CH_3OH)]\cdot CH_3COCH_3$ (fw = 1605.89): C, 61.33; H, 4.14; N, 1.74; (fresh sample) Found: C, 61.29; H, 4.10; N, 1.71%. IR (cm^{-1}): 3058w, 1596s, 1551s, 1520s, 1478s, 1403s, 1313m, 1222w, 1104m, 1024w, 786w, 729w, 689w, 609w.

Single-crystal X-raystructure determination.

The single-crystal X-ray diffraction data for complexes **1**–**5** were collected using a BRUKER SMART-1000 CCD diffractometer equipped with graphite-monochromatized Mo-Kα radiation with a radiation wavelength of 0.071073 nm using the ω-φ scan technique. The structures were solved by direct methods using the program SHELXS-97,[15] and refined anisotropically using the full-matrix least-squares technique based on F^2 using SHELXL-97.[15] Anisotropic thermal parameters were assigned to all non-hydrogen atoms. The hydrogen atoms were generated geometrically. Crystal data collection and refinement details for complexes **1**–**5** are summarized in Table 1.

Table 1 Crystal data and structure refinement for complexes **1–5**

Complex	**1**	**2**	**3**	**4**	**5**
Formula	$C_{80}H_{64}N_2Nd_2O_{12}$	$C_{80}H_{64}N_2O_{12}Tb_2$	$C_{80}H_{64}Dy_2N_2O_{12}$	$C_{80}H_{64}Ho_2N_2O_{12}$	$C_{82}H_{66}Er_2N_2O_{12}$
Formula weight	1533.81	1563.17	1570.34	1575.2	1605.89
Temperature (K)	113(2)	113(2)	113(2)	113(2)	113(2)
Wavelength (Å)	0.71073	0.71073	0.71073	0.71073	0.71073
Crystal system	Triclinic	Triclinic	Triclinic	Triclinic	Triclinic
Space group	$P\bar{1}$	$P\bar{1}$	$P\bar{1}$	$P\bar{1}$	$P\bar{1}$
a (Å)	10.398(2)	10.371(2)	10.353(2)	10.345(2)	11.064(2)
b (Å)	15.380(3)	11.930(2)	11.927(2)	11.963(2)	18.015(4)
c (Å)	21.470(4)	15.273(3)	15.210(3)	15.200(3)	18.101(4)
α (deg)	100.71(3)	96.82(3)	97.05(3)	96.96(3)	87.10(3)
β (deg)	91.19(3)	98.56(3)	98.50(3)	98.56(3)	76.30(3)
γ (deg)	98.85(3)	115.13(3)	115.22(3)	115.21(3)	78.86(3)
Volume (Å^3)	3329.4(12)	1656.4(5)	1643.9(6)	1646.8(6)	3439.3(12)
Z	2	1	1	1	2
Calculated density (Mg m^{-3})	1.530	1.567	1.586	1.588	1.551
Absorption coefficient (mm^{-1})	1.609	2.185	2.323	2.453	2.490
F (000)	1548	784	786	788	1608
θ range for data collection (deg)	1.82 to 25.02	1.93 to 25.02	1.93 to 25.00	2.13 to 25.00	1.15 to 25.02
Reflections collected	34727	13912	13619	13902	34518
Independent reflection	11762 [R(int) = 0.0387]	5824 [R(int) = 0.0325]	5737 [R(int) = 0.0323]	5785 [R(int) = 0.0402]	12097[R(int)=0.0580]
Completeness	99.9 %	99.4%	98.9 %	99.6 %	99.6 %
Max. and min. transmission	0.9096 and 0.8303	0.7795 and 0.6691	0.7679 and 0.6537	0.7573 and 0.6145	0.7543 and 0.6358
Data / restraints / parameters	11762 / 0 / 867	5824 / 236 / 455	5737 / 150 / 488	5785 / 150 / 488	12097 / 0 / 885
Goodness-of-fit on F^2	1.025	1.074	1.225	1.134	1.076
Final R indices [I>2σ(I)]	R_1 = 0.0341, wR_2 = 0.0770	R_1 = 0.0294, wR_2 =0.0673	R_1 = 0.0275, wR_2 = 0.0759	R_1 = 0.0296, wR_2 = 0.0703	R_1 = 0.0400, wR_2 = 0.0954
R indices (all data)	R_1 = 0.0445, wR_2 = 0.0830	R_1 = 0.0324, wR_2 = 0.0689	R_1 = 0.0308, wR_2 = 0.0879	R_1 = 0.0345, wR_2 = 0.0872	R_1 = 0.0491, wR_2 = 0.1077
Largest diff. peak and hole(e Å^{-3})	0.874 and -1.179	0.871 and -1.012	1.286 and -1.179	1.522 and -1.303	2.225 and -1.840

Results and discussion

Crystal structure descriptions.

Crystal structure of complex **1**

Single-crystal X-ray diffraction analysis reveals that complex **1** crystallizes in the triclinic $P\bar{1}$ space group. A perspective view of the molecular structure of **1** is represented in Fig. 1. The two Nd^{III} ions are all eight-coordinated by four oxygen atoms from two dbm anions, two oxygen atoms from the bridging OQ ligands, another oxygen atom from coordinated methanol molecule and one nitrogen atom from the quinoline ring. The bond lengths of the Nd–O are in the range of 2.382(2)–2.537(3) Å and the Nd–N bond lengths are 2.593(3) and 2.580(3) Å for complex **1**. Two Nd^{III} ions are bridged by the μ-phenol atoms (O1 and O2) from OQ ligands, with four Nd–O bond lengths of Nd1−O1 2.449(2) Å, Nd2−O1 2.430(2) Å, Nd1−O2 2.461(2) Å, and Nd2−O2 2.449(2) Å, and Nd···Nd distance of 4.0192(16) Å. The bridging angles of Nd1−O1−Nd2 and Nd1−O2−Nd2 are 110.91(9) and 109.88(9)°, respectively. The evaluation of the polyhedral shapes of the two Nd^{III} centers were ascertained by continuous shape measurement analysis that was carried out with SHAPE 2.[16] Here, the eight-coordinated Nd1 and Nd2 centers were found to close to the triangular square antiprism (SAPR-8) with values of 0.920 and 1.586 respectively. The larger value exhibits a distorted coordination polyhedron that deviates from ideal geometries. The selected bond lengths and angles for complex **1** are summarized in Tables **S1** in the ESI.

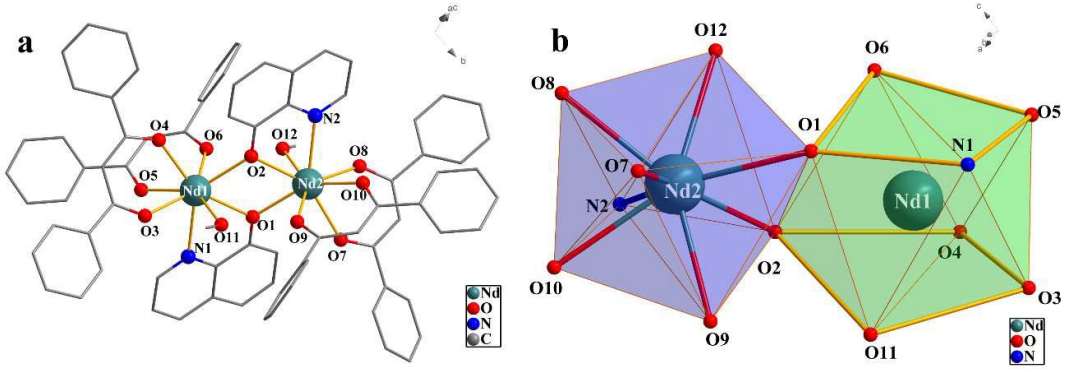

Fig. 1. (a) Molecular structure of complex **1**. Hydrogen atoms have been omitted for clarity. **(b)** The

coordination geometries of Nd1 and Nd2 atoms in complex **1**.

Crystal structures of complexes **2**−**4**

X-ray crystallographic analysis reveals that **2**−**4** are isomorphic dinuclear complexes and crystallize in the triclinic $P\bar{1}$ space group. Therefore, as a representative, only the structure of complex **3** is discussed in detail. As shown in Fig. 2, the asymmetric unit is composed of two crystallographically independent $[Dy_2(dbm)_4(OQ)_2(CH_3OH)_2]$ moieties. Each moiety contains two eight-coordinated Dy^{III} cations, four dbm and two 8-quinolinolate ligands and two methanol molecules. The coordination and bridging models of centre Dy^{III} ions are similar as Nd^{III} ions in complex **1**. The slight difference of **1** and **3** is that one of the two Dy^{III} ions was generated by symmetric operation in the asymmetric unit, while one of the two Nd^{III} ions cannot generate by symmetric operation.

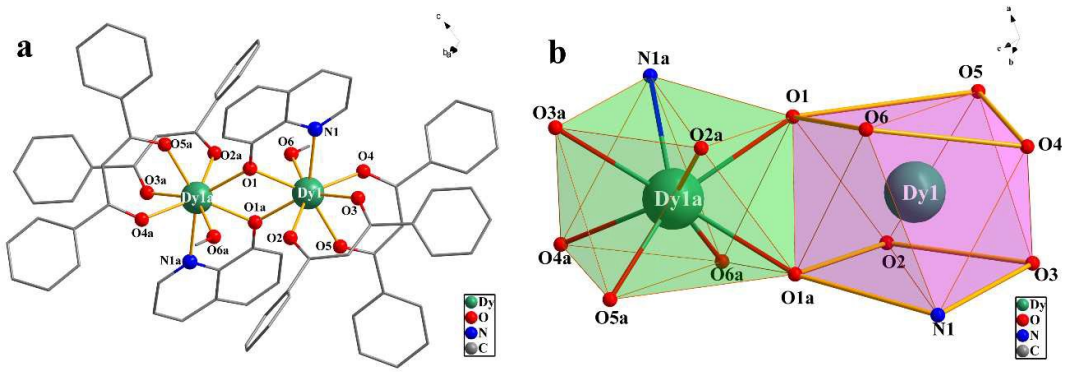

Fig. 2. (a) Molecular structure of complex **3**. Hydrogen atoms have been omitted for clarity. **(b)** The coordination geometries for the Dy1 and Dy1a atoms in complex **3**.

Crystal structure of complex **5**

Single-crystal X-ray diffraction analysis reveals that complex **5** crystallizes in the triclinic $P\bar{1}$ space group and consists of a discrete neutral $[Er_2(dbm)_4(OQ)_2(CH_3OH)]$ entity and an acetone molecule as cocrystallizing solvent. A perspective view of the molecular structure of **5** without the solvent molecules is represented in Fig. 3. The Er1 ion is eight-coordinated by two N atoms and two μ-phenol oxygen atoms from the bridging OQ ligands and four oxygen

atoms from two dbm anions, while the Er2 ion is seven-coordinated by four oxygen atoms from two dbm anions, two oxygen atoms from the bridging OQ ligands, another oxygen atom from coordinated methanol molecule. Er1 and Er2 are bridged by two μ-phenol oxygen atoms (O1 and O2) of two ligands, leading to a four-membered Er_2O_2 core. In the bridging path ways, the Er–O lengths are 2.309(3) Å for Er1–O1, 2.344(3) Å for Er2–O1, 2.282(3) Å for Er1–O2, 2.350(3) Å for Er2–O2, respectively. The Er–O–Er angles are 109.03(12)° for Er1–O1–Er2, and 109.74(13)° for Er1–O2–Er2. Systematic analysis of the coordination geometries around the metals using the program SHAPE 2 reveals that Er1 ion adopts a distorted capped octahedron with a C_{3v} point group, while Er2 ion has geometry close to triangular dodecahedron (TDD-8) with a D_{2d} point group.

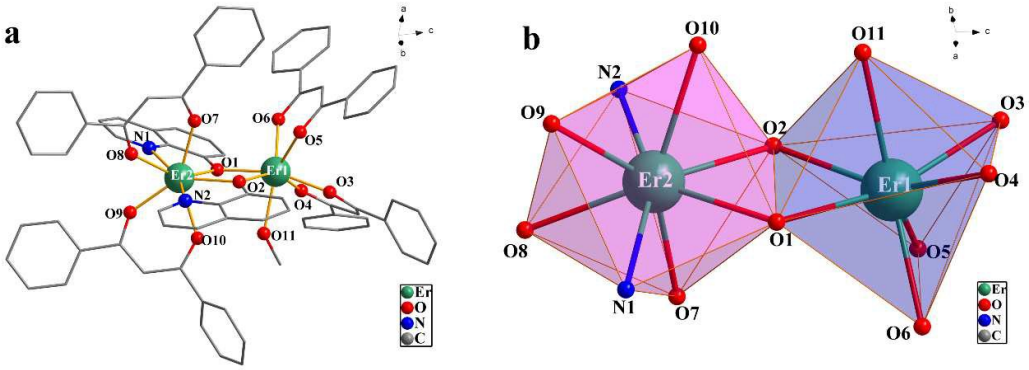

Fig. 3. (a) Molecular structure of complex **5**. Hydrogen atoms have been omitted for clarity. **(b)** The coordination geometries for the Er1 and Er2 atoms in complex **5**.

Thermal gravimetric analysis and powder X-ray diffraction

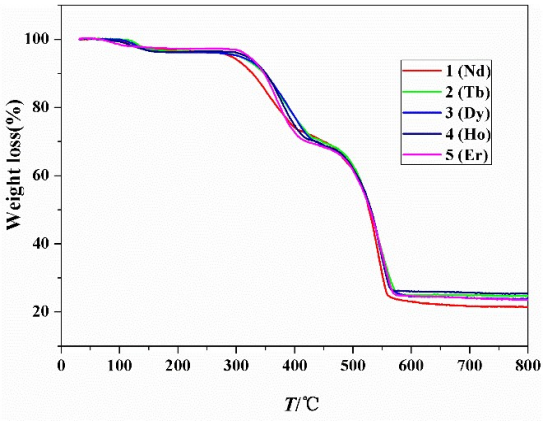

Fig. 4. TGA curves for complexes **1**–**5**.

To identify the thermal stabilities of these complexes, thermal gravimetric analyses of complexes **1–5** were carried out under air atmosphere with a heating rate of 10 °C min^{-1} in the temperature range of 30 to 800 °C. TGA curves of **1**–**5** (Fig. 4) have similar profiles, exhibiting two main weight loss steps until the decomposition of the framework. Therefore, as a representative, only the TGA curve of **1** is discussed in detail. In the TGA curve of **1**, the first weight loss of 3.35% in the range of 90–180 °C corresponds to the departure of two coordinated methanol molecules (calcd: 4.05%). Then, the skeleton of **1** can be stable up to about 250 °C. As the temperature continues to rise, the framework decomposes gradually. Finally, the residue of 21.54% (calcd. 21.94%) is expected to be the corresponding lanthanide oxide Nd_2O_3. For **5**, one lattice acetone molecule is uncoordinated and the crystalline samples were kept for a period of time at ambient conditions resulting in the acetone molecules losing spontaneously, so there are no solvent loss occurs in the 30–100 °C range.

The crystalline products of **1**–**5** were characterized using X-ray powder diffraction (PXRD) at room temperature (Fig. S1–S3). These results are in good agreement with the XRD patterns simulated from the single-crystal data, indicating high purity of the obtained samples. The differences in intensity may be due to the preferred orientations of the crystalline powder samples.

UV-vis spectra.

The UV-vis absorption spectra of $Dy(dbm)_3{\cdot}2H_2O$, the ligand and complexes **1**–**5**, recorded in CH_3OH solution of 10^{-5} mol·L^{-1} at room temperature, are depicted in Fig. 5. The absorption spectrum of the HOQ ligand features three main bands located around 240, 256, 310 nm respectively with absorption extending up to 350 nm. They are assigned to $\pi\rightarrow\pi^*$ and $n\rightarrow\pi^*$ transitions. $Dy(dbm)_3{\cdot}(H_2O)_2$ has two absorption bands centered ca. 250 nm and 350 nm. Upon deprotonation and the formation of complex, the absorption bands are slightly

red-shifted. In the UV-vis spectra of **1**–**5**, there are two sets of absorption bands. The high-energy band at *ca.* 256 nm results from the intraligand $\pi \rightarrow \pi^*$ transition of HOQ and dbm ligands. The other absorption band at *ca.* 355 nm arises probably from the $n \rightarrow \pi^*$ of dbm ligands.

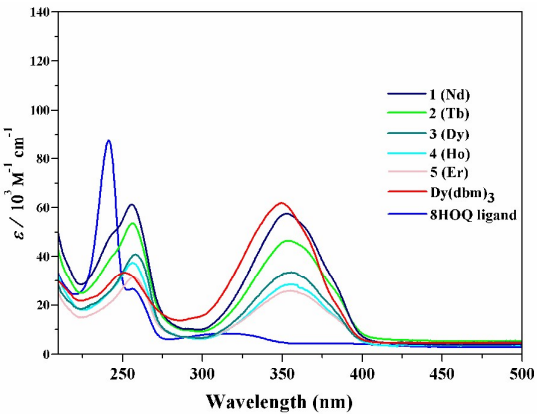

Fig. 5. UV-vis absorption spectra of complexes **1**–**5** in CH_3OH solution at room temperature.

Room-temperature UV-Vis absorption spectra of the complexes were also determined in the solid state (Fig. S4). The HOQ ligand and $Dy(dbm)_3 \cdot (H_2O)_2$ show wide absorption bands between 200-400 nm and 200-420 nm, respectively. The spectra of the complexes all exhibit broad absorption bands in the range from 200 to 410 nm, which could correspond to the intraligand π-π* transition of the organic ligands. In the region above 420 nm in these curves, **1**, **4** and **5** also show characteristic absorption bands of corresponding lanthanide ions. The absorption spectra of **1**, in the visible region, contain six transitions originating from the $^4I_{9/2}$ ground state to the excited states. These are assigned to $^4I_{9/2} \rightarrow {}^4G_{9/2}$ (515 nm), $^4I_{9/2} \rightarrow {}^4G_{7/2}$, $^2K_{13/2}$ (526 nm), $^4I_{9/2} \rightarrow {}^2G_{7/2}$(582 nm), $^4I_{9/2} \rightarrow {}^2H_{11/2}$ (628 nm), $^4I_{9/2} \rightarrow {}^4F_{9/2}$ (680 nm) and $^4I_{9/2} \rightarrow {}^4F_{7/2}$ (745 nm). The spectra of the **4** show four transitions originating from the $^5I_8$ ground state to various excited states of Ho^{III}. These f–f transitions correspond to $^5I_8 \rightarrow {}^5G_6 + {}^5F_1$ (451 nm), $^5I_8 \rightarrow {}^5F_3$ (483 nm), $^5I_8 \rightarrow {}^5F_4$ (538 nm) and $^5I_8 \rightarrow {}^5F_5$ (641 nm). Similarly, the f–f transitions observed in the case of erbium complex correspond to $^4I_{15/2} \rightarrow {}^4F_{7/2}$ (486 nm), $^4I_{15/2}$

$\rightarrow {}^2H_{11/2}$ (520 nm), ${}^4I_{15/2} \rightarrow {}^4S_{3/2}$ (544 nm) and ${}^4I_{15/2} \rightarrow {}^4F_{9/2}$ (652 nm).[17]

Near-infrared luminescent properties.

The NIR luminescent properties of complex **1** in the solid state were investigated at room temperature. The excitation spectra were obtained by monitoring the strongest emission of the Nd^{III} ion at 1060 nm (Fig. S5). The broad band ranging from 300 to 600 nm and several weak intra configurational f−f transitions of the excitation spectra can be observed. The broad band is attributed to intraligand charge transfer (ILCT) and weak intraconfigurational f−f transitions originating from the ground states of Nd^{III} ion. The f−f transitions could be assigned to ${}^4I_{9/2} \rightarrow {}^4G_{7/2}$ (528 nm) and ${}^4I_{9/2} \rightarrow {}^4G_{5/2}$, ${}^2G_{7/2}$ (586 nm).[18] The excitation spectra are dominated by the broad band as compared to weak intraconfigurational f−f transitions, which indicates that luminescence sensitization is efficient via excitation of the ligands.

For Nd^{III} complex, the emission spectrum displays three bands in the 850–1400 nm range, the main band occurring between 1020 and 1120 nm (${}^4F_{3/2} \rightarrow {}^4I_{11/2}$), with a maximum at 1060 nm; two other bands are visible between 850–928 (${}^4F_{3/2} \rightarrow {}^4I_{9/2}$) and 1300–1400 nm (${}^4F_{3/2} \rightarrow {}^4I_{13/2}$).[18-19] Among the three emission bands, the band centered at 1060nm shows the strongest intensity, which is potentially applicable for the laser system.[20] The commonly accepted energy transfer pathway for the sensitization of Ln^{III} ion luminescence is that the ligand-to-metal energy transfer from the lowest triplet level of ligand to an excited state of lanthanide ion through a nonradiative transition.[21] To make energy transfer effective, the triplet states of the ligand and the accepting lanthanide energy level should be matched. In this paper, the triplet energy levels of the 8HOQ and dbm ligands are 17100 cm^{-1} and 20520 cm^{-1}, which all lie above the emitting level (${}^4F_{3/2}$) of Nd^{III}. Therefore, both ligands can effectively transfer energy to the ${}^4F_{3/2}$ emitting level of the Nd^{III} ion. The NIR emission dynamics of complex 1 excited at 355nm is reported in Fig. S6. The luminescence decay is a single exponential function, indicating the presence of only one emitting neodymium center

in the solid state. The observed luminescence lifetimes is 0.142 μs.

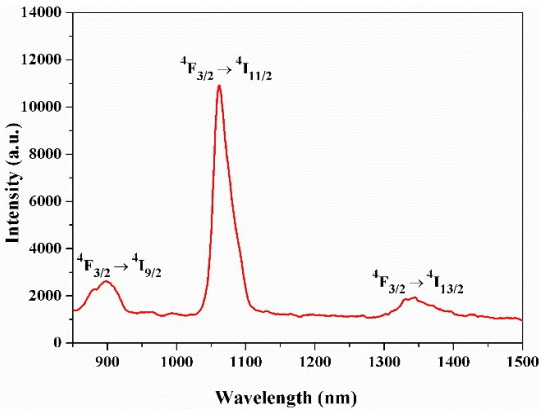

Fig. 6. The NIR emission spectrum of complex **1** in the solid-state at room-temperature under 355 nm excitation.

Magnetic properties

Static magnetic susceptibility. Variable-temperature dc magnetic susceptibility studies were performed on polycrystalline samples of complexes **1**−**5** under an applied magnetic field of 1000 Oe over the temperature range 300–2 K, as shown in Fig. 7. The $\chi_M T$ values at room temperature for **1-5** are found to be 2.75, 23.21, 27.65, 27.29, and 22.22 cm^3 K mol^{-1}, respectively. In each case, this value is close to the theoretical values for two isolated Ln^{III} cations follow: two Nd^{III} ($^4I_{9/2}$) are 3.28 cm^3 K mol^{-1} for **1**, two Tb^{III} ($^7F_6$, $g = {}^3/_2$) are 23.64 cm^3 K mol^{-1} for **2**; two Dy^{III} ($^6H_{15/2}$, $g = {}^4/_3$) are 28.34 cm^3 K mol^{-1} for **3**; two Ho^{III} ($^5I_8$, $g = {}^5/_4$) are 28.14 cm^3 K mol^{-1} for **4**; and two Er^{III} ($^4I_{15/2}$, $g = {}^6/_5$) are 22.96 cm^3 K mol^{-1} for **5**.[22] These values indicate that the magnetic exchange is weak as expected because of the shielded nature of the 4f orbitals.

When the temperature is lowered, $\chi_M T$ values of **1** decrease to 1.35 cm^3 K mol^{-1} at 2.0 K, the thermal variations of $\chi_M T$ are almost constant over the whole temperature range, being similar to those of previous reports. For complex **2**, as the temperature decreases, the $\chi_M T$ value decreases slowly and almost remains constant until *ca*. 40 K. On further cooling, an upturn in $\chi_M T$ observed below 18 K, reaching a value of 24.11 cm^3 K mol^{-1} at 2 K. The small

low temperature increase suggests that the existence of weak ferromagnetic interactions between the Tb^{III} ions. For **3**–**5**, during the cooling process, the $\chi_M T$ values experience almost no change over the temperature range of 300–100 K, which indicates competitive balance between ferromagnetic interactions and thermal depopulation of the Stark sublevels,[23] and then further decrease to reach minima of 23.63 (**3**), 20.52 (**4**), 9.11 (**5**) cm^3 K mol^{-1} at 2 K.

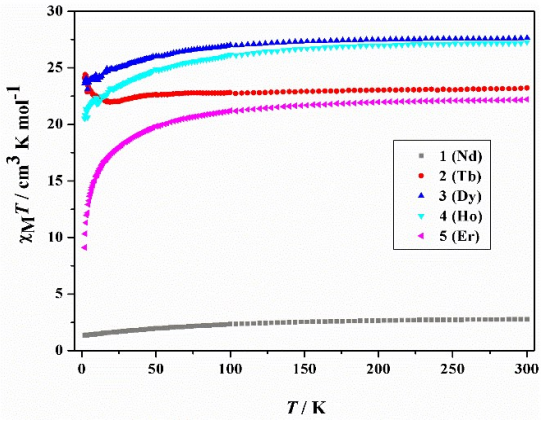

Fig. 7. Temperature dependence of the $\chi_M T$ products in 1000 Oe for complexes **1–5**.

Dynamic magnetic properties. To investigate the dynamics of the magnetization which may originate from a single-molecule magnet, alternating current (ac) susceptibility measurements at different temperatures under a zero dc field in an oscillating ac field of 3 Oe with frequencies ranging between 111 and 2311 Hz were performed. The ac magnetic susceptibilities (Fig. 8) showed that complex **3** exhibits no obvious frequency dependence in-phase (χ') signals but present frequency-dependent signals of out–of–phase observed at zero dc field. Furthermore, a slight shoulder structure around 10 K which can be more visible in the out-of-phase component χ''. These data are indicative of the slow magnetization relaxation process and suggest possible SMM behavior with a small energy barrier for magnetization reversal. However, there is no maxima in the out-of-phase ac susceptibility data observed. This behavior reveals that the slow relaxation of the magnetization is highly influenced by a fast quantum tunneling relaxation of the magnetization (QTM) through the spin reversal barrier.[24] These phenomena were commonly observed in lanthanide SMMs.[25] To

partially or fully suppress the quantum tunneling process, ac susceptibility measurements were carried out with the application of a 3000 Oe dc field on a polycrystalline sample of **3**, where the in-phase and out-of-phase curves show clear frequency-dependent signals and give good peak shapes below 12 K as shown in Fig.9, clearly suggesting a slow relaxation of magnetization. This confirms the presence of significant QTM, and thus, complex **3** can be considered as a field-induced SMM.

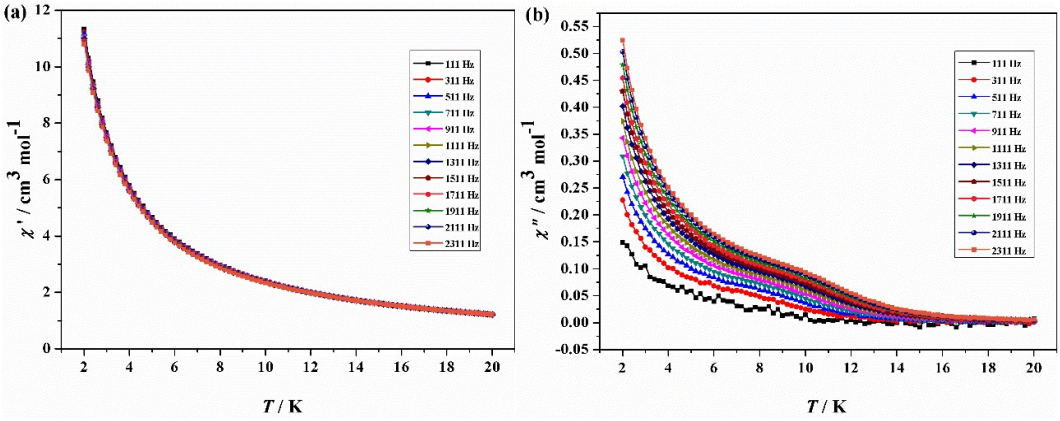

Fig. 8. Temperature dependence of the in-phase (χ′) and out-of phase (χ″) ac susceptibility of **3** under zero dc field.

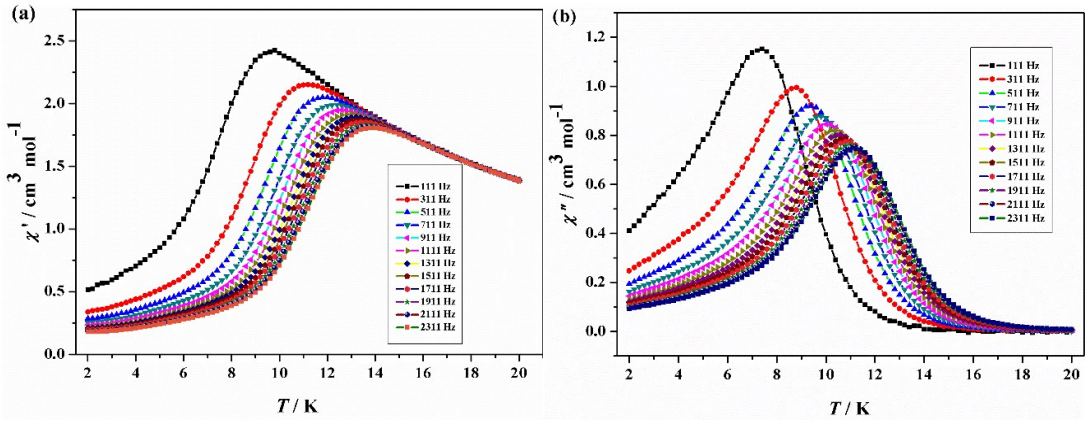

Fig. 9. Temperature dependence of the in-phase (χ′) and out-of phase (χ″) ac susceptibility of **3** with a 3000 Oe dc field.

To further probe the dynamics of **3**, frequency dependencies of the alternating-current (ac) susceptibility under a 3000 Oe dc field in an oscillating ac field of 3 Oe are carried out (Fig. 10). Using the frequency dependencies of the ac susceptibility, the magnetization relaxation

times (τ) were estimated between 5.5 and 12.5 K (Fig. 11). The relaxation energy barrier can be obtained by fitting τ values based on the Arrhenius equation $\tau = \tau_0 \exp(-\Delta E/k_B T)$, giving the energy barrier $\Delta E/k_B$ = 109.5 K with the pre-exponential factor $\tau_0 = 4.23\times10^{-9}$ s. The result of τ_0 is consistent with the expected value of 10^{-6}–10^{-12} s and comparable to those of reported SMMs.[26] Below 10.0 K, the deviation from the linear relation of relaxation times indicating a gradual crossover from a thermally activated Orbach mechanism that is predominant at higher temperatures, to a QTM in the doublet ground state.[27]

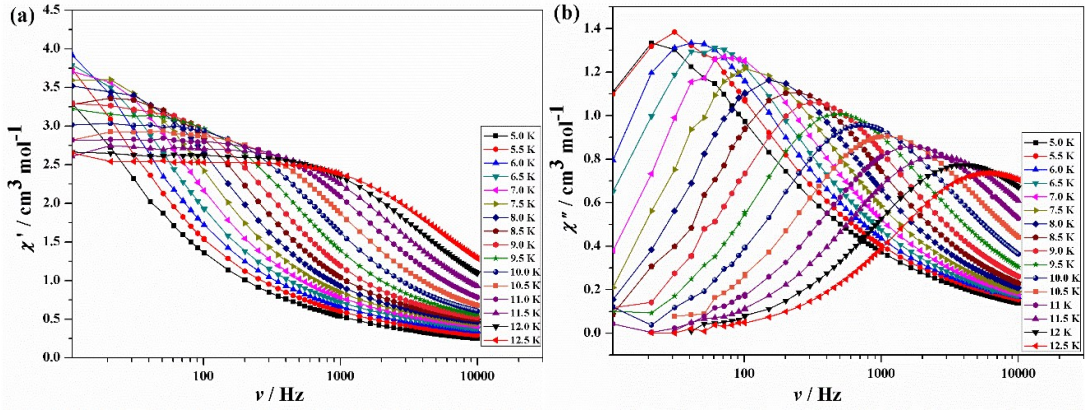

Fig. 10. Frequency dependence of ac susceptibilities for complex **3** under 3000 Oe dc field (H_{ac} = 3Oe).

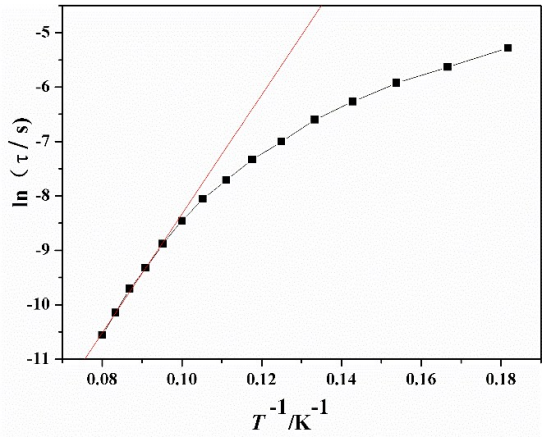

Fig. 11. Magnetization relaxation time, ln(τ) vs T^{-1} plot under H_{dc}= 3000 Oe; the red line is fitted with the Arrhenius equation.

Using the frequency dependences of the ac susceptibility measurements, the Cole-Cole plots of χ'' *vs* χ' for **3** (Fig. 12) were obtained and fitted to the generalized Debye model to

obtain the α values in the range of 0.12–0.49. This suggests a relatively wide distribution of the relaxation time and the presence of more than one relaxation process in the dysprosium complex. The change of the circle from unsymmetric to symmetric is similar to those of some reported dysprosium SMMs with different coordination geometries around the Dy^{III} centers.[28]

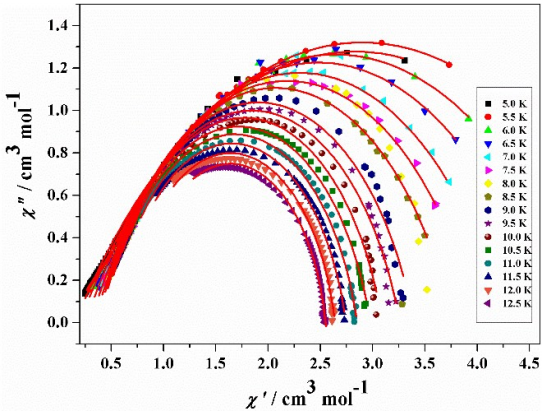

Fig. 12. Cole-Cole plots for **3**. The solid lines are the best fits to the experimental data obtained using the generalized Debye model.

The indicative parameter of the spin disorder φ of 0.26 can be extracted based on the Mydosh formula $\varphi = (\Delta T_p/T_p)/\Delta(\log\omega)$ [29] and falls into the normal range ($0.1 < \varphi < 0.3$)[29-30] expected for a super-paramagnet, which suggested the magnetic behavior of complex **3** could not originate spin glass behavior.

For lanthanide-based complexes, slow magnetic relaxation is often attributed to single-ion factors rather than magnetic exchange and proceeds through thermal relaxation of the lowest excited states. Dy^{III} is a Kramer ion and possess a usually large ground Kramers doublet with M_J = 15/2 and the complexity of the relaxation phenomena is related to the number of relaxation paths available (reversal mechanism via quantum tunnelling of magnetization within the lowest energy doublet, thermal mechanism via an excited state, thermally activated quantum tunnelling of magnetization occurring within an excited doublet).[31] In this paper, upon application of higher static fields, the quantum tunnelling of magnetization (QTM)

process can be reduced, and the paths, such as the Orbach process, mainly govern the dynamics of the two-level systems.

To investigate magnetization dynamics of the Tb^{III}, complex **2** was also studied in the temperature (2 −20 K) and frequency dependence (111−2311 Hz) modes by measuring the ac magnetic susceptibilities in the absence of an applied dc magnetic field (Fig. S5). Complex **2** displayed no observable out-of-phase signal revealing its non SMM behavior. The difference in the magnetic behavior of the Dy^{III} and Tb^{III} complexes in the present study may be related to the electronic structure of these ions due to ligand-field splitting.[32] Dy^{III} is a Kramer ion and therefore always has a bistable ground state, as is necessary contribution to SMM behavior, irrespective of the symmetry of the coordination environment.[33] Comparing with Dy^{III} ion, the Tb^{III} ion is a non-Kramer ion, so its complex will possess a bistable ground state only if it is present in a highly axial symmetry ligand field.

Conclusions

In summary, five new lanthanide complexes were synthesized using 8-hydroxyquinoline and dibenzoylmethanate as ligands. These compounds are μ-phenol bridged dinuclear complexes. Complex **1** shows the characteristic peaks of Nd^{III} ions in the NIR region, which indicates that efficiency of the energy transfer from the ligands to the ions is ideal. Dynamic magnetic studies reveal that complex **3** exhibits the slow relaxation of the magnetization and this behavor is highly influenced by a fast quantum tunneling relaxation of the magnetization (QTM). In comparison with complex **3**, complex **2** exhibits weak ferromagnetic interactions and does not show slow relaxation of magnetization. The difference in the magnetic behavior of the Dy^{III} and Tb^{III} complexes in the present study may be related to the electronic structure of these ions due to ligand-field splitting.

Acknowledgments

This work was financially supported by the National Natural Science Foundation of China

(Nos. 21473121, 21271137, 21571138).

References

[1] (*a*) N. Domingo, E. Bellido and D. Ruiz-Molina, *Chem. Soc. Rev.*, 2012, **41**, 258; (*b*) S. Sanvito, *Chem. Soc. Rev.*, 2011, **40**, 3336.

[2] F. Troiani and M. Affronte, *Chem. Soc. Rev.*, 2011, **40**, 3119.

[3] (*a*) J. Camarero and E. Coronado, *J. Mater. Chem.*, 2009, **19**, 1678; (*b*) Y.-Z. Zheng, G.-J. Zhou, Z.-P. Zheng and R. E. P. Winpenny, *Chem. Soc. Rev.*, 2014, **43**, 1462.

[4] (*a*) V. Chandrasekhar, S. Das, A. Dey, S. Hossain and J.-P. Sutter, *Inorg. Chem.*, 2013, **52**, 11956; (*b*) A. K. Jami, V. Baskar and E. C. Sañudo, *Inorg. Chem.*, 2013, **52**, 2432; (*c*) S. Das, A. Dey, S. Biswas, E. Colacio and V. Chandrasekhar, *Inorg. Chem.*, 2014, **53**, 3417.

[5] M. Yadav, V. Mereacre, S. Lebedkin, M. M. Kappes, A. K. Powell and P. W. Roesky, *Inorg. Chem.*, 2015, **54**, 773.

[6] N. Ishikawa, M. Sugita, T. Ishikawa, S.-Y. Koshihara and Y. Kaizu, *J. Am. Chem. Soc.*, 2003, **125**, 8694.

[7] (*a*) L. Zhang, P. Zhang, L. Zhao, J.-F. Wu, M. Guo and J.-K. Tang, *Inorg. Chem.*, 2015, **54**, 5571; (*b*) J. D. Rinehart and J. R. Long, *Chem. Sci.*, 2011, **2**, 2078.

[8] (*a*) S. Zhang, H.-S. Ke, X.-Y. Liu, Q. Wei, G. Xie and S.-P Chen, *Chem. Commun.*, 2015, **51**, 15188; (*b*) P.-H. Guo, J. Liu, Z.-H. Wu, H. Yan, Y.-C. Chen, J.-H. Jia and M.-L. Tong, *Inorg. Chem.*, 2015, **54**, 8087.

[9] (*a*) F. Habib and M. Murugesu, *Chem. Soc. Rev.*, 2013, **42**, 3278; (*b*) F. Tuna, C. A. Smith, M. Bodensteiner, L. Ungur, L. F. Chibotaru, E. J. L. McInnes, R. E. P. Winpenny, D. Collison and R. A. Layfield, *Angew. Chem. Int. Ed.*, 2012, **51**, 6976; (*c*) L. Ungur, S.-Y. Lin, J.-K. Tang and L. F. Chibotaru, *Chem. Soc. Rev.*, 2014, **43**, 6894; (*d*) N. M. Randell, M. U. Anwar, M. W. Drover, L. N. Dawe and L. K. Thompson, Inorg. Chem., 2013, **52**, 6731; (*e*) N. F. Chilton, D. Collison, E. J. L. McInnes, R. E. P. Winpenny and A. Soncini, *Nat. Commun.*, 2013, **4**, 2551; (*f*) H.-H. Zou, L.-B. Sheng, Z.-L. Chen and F.-P. Liang, *Polyhedron*, 2015, **88**, 110; (*g*) B. Joarder, S. Mukherjee, S. Xue, J. Tang and S. K. Ghosh, *Inorg. Chem.,* 2014, **53**, 7554; (*h*) S.-Y. Lin, J.-K. Tang, *Polyhedron*, 2014, **83**, 185.

[10] S.-Y. Lin, X.-L. Li, H.-S. Ke and Z.-K. Xu, *CrystEngComm.*, 2015, **17**, 9167.

[11] (*a*) J.-J. Shi, C.-H. Gong, X.-H. Zeng, J.-Y. Zhang, C.-F. Zhu and J.-L. Xie, *Polyhedron*, 2015, **102**, 562; (*b*) C.-F. Leung, S.-M. Ng, J. Xiang, W.-Y. Wong, M. Hon-Wah Lam, C.-C. Ko and T.-C. Lau, *Organometallics*, 2009, **28**, 5709; (*c*) L.-X. Ning, M. I. Trioni and G. P. Brivio, *J. Mater. Chem.*, 2007, **17**, 4464.

[12] C.W. Tang and S. A. Vanslyke, *Appl. Phys. Lett.*, 1987, **51**, 913.

[13] (*a*) G. Bozoklu, C. Marchal, J. Pécaut, D. Imbert and M. Mazzanti, *Dalton Trans.*, 2010, **3**9, 9112; (*b*) H.-B. Xu, J. Li, L.-X. Shi and Z.-N. Chen, *Dalton Trans.*, 2011, **40**, 5549.

[14] (*a*) H.-Y. Shen, W.-M. Wang, Y.-X. Bi, H.-L. Gao, S. Liu and J.-Z. Cui, *Dalton Trans.*, 2015, **44**, 18893; (*b*) W.-M. Wang, H.-X. Zhang, S.-Y. Wang, H.-Y. Shen, H.-L. Gao, J.-Z. Cui and B. Zhao, *Inorg. Chem.*, 2015, **54**, 10610; (*c*) W.-M. Wang, S.-Y. Wang, H.-X. Zhang, H.-Y. Shen, J.-Y. Zou, H.-L.

Gao, J.-Z. Cui and B. Zhao, *Inorg. Chem. Front.*, 2016, **3**, 133.

[15] G. M. Sheldrick, *SHELXS-97*, Program for the Solution of Crystal Structures; University of Göttingen: Göttingen, Germany, 1997.

[16] (*a*) SHAPE, version 2.0; continuous shape measures calculation; Electronic Structure Group, Universitat de Barcelona: Barcelona, Spain, 2010; (*b*) D. Casanova, M. Llunell, P. Alemany and S. Alvarez, *Chem.-Eur. J.*, 2005, **11**, 1479.

[17] L.-N. Sun, J.-B. Yu, G.-L. Zheng, H.-J. Zhang, Q.-G. Meng, C.-Y. Peng, L.-S. Fu, F.-Y. Liu and Y.-N. Yu, *Eur. J. Inorg. Chem.,* 2006, **19**, 3962.

[18] Z. Ahmed and K. Iftikhar, *J. Phys. Chem. A*, 2013, **117**, 11183.

[19] L.-N. Sun, Y.-N. Qiu, T. Liu, J.-Z. Zhang, S. Dang, J. Feng, Z.-J. Wang, H.-J. Zhang and L.-Y. Shi, *ACS Appl. Mater. Interfaces*, 2013, **5**, 9585.

[20] (*a*) L.-N. Sun, S. Dang, J.-B. Yu, J. Feng, L.-Y. Shi and H.-J. Zhang, *J. Phys. Chem. B*, 2010, **114**, 16393; (*b*) L.-N. Sun, X.-Q. Ge, J.-L. Liu, Y.-N. Qiu, Z.-W. Wei, B. Tian and L.-Y. Shi, *Nanoscale*, 2014, **6**, 13242.

[21] G. A. Crosby, R. M. Alire and R. E. Whan, *J. Chem. Phys.*, 1961, **34**, 743.

[22] D. Aguilà, L. A. Barrios, V. Velasco, L. Arnedo, N. Aliaga-Alcalde, M. Menelaou, S. J. Teat, O. Roubeau, F. Luis and G. Aromí, *Chem. – Eur. J.*, 2013, **19**, 5881.

[23] W.-T. Xu, Y.-F. Zhou, D.-C. Huang, W. Xiong, M.-Y. Su, K. Wang, S. Han and M.-C. Hong, *Cryst. Growth Des.*, 2013, **13**, 5420.

[24] S. Bala, M. S. Bishwas, B. Pramanik, S. Khanra, K. M. Fromm, P. Poddar and R. Mondal, *Inorg. Chem*., 2015, **54**, 8197.

[25] (*a*) Y.-L. Chien, M.-W. Chang, Y.-C. Tsai, G.-H. Lee, W.-S. Sheu and E.-C. Yang, *Polyhedron*, 2015,**102**, 8; (*b*) M. Fang, X.-H. Li, P. Cui and B. Zhao, *Journal of Solid State Chemistry*, 2015, **223**, 138; (*c*)Y. Li , J. -W. Yu, Z.-Y. Liu, E.-C. Yang and X. -J. Zhao, *Inorg. Chem.*, 2015, **54**, 153.

[26] (*a*) P. Zhang, L. Zhang and J.-K. Tang, *Dalton Trans.,* 2015, 44, 3923; (*b*) K. Suzuki, R. Sato and N. Mizuno, *Chem. Sci.*, 2013, **4**, 596; (*c*) P. Bag, C. K. Rastogi, S. Biswas, S. Sivakumar, V. Mereacre and V. Chandrasekhar, *Dalton Trans.,* 2015, **44**, 4328.

[27] (*a*) H.-S. Ke, S. Zhang, X. Li, Q. Wei, G. Xie, W.-Y. Wang and S.-P. Chen, *Dalton Trans.*, 2015, **44**, 21025; (*b*) X.-J. Zhang, V. Vieru, X.-W. Feng, J.-L. Liu, Z.-J. Zhang, B. Na, W. Shi, B.-W. Wang, A. K. Powell, L. F. Chibotaru, S. Gao, P. Cheng and J. R. Long, *Angew. Chem., Int. Ed.*, 2015, **54**, 9861.

[28] F. Luan, P.-F. Yan, J. Zhu, T.-Q. Liu, X.-Y. Zou and G.-M. Li, *Dalton Trans.*, 2015, **44**, 4046.

[29] J. A. Mydosh, Spin Glasses: An Experimental Introduction, Taylor & Francis, London, 1993.

[30] N. Ishii, Y. Okamura, S. Chiba, T. Nogami and T. Ishida, *J. Am. Chem. Soc.*, 2008, **130**, 24.

[31] N. C. Anastasiadis, D. A. Kalofolias, A. Philippidis, S. Tzani, C. P. Raptopoulou, V. Psycharis, C. J. Milios, A. Escuer and S. P. Perlepes, *Dalton Trans.*, 2015, **44**, 10200.

[32] Y. Horii, K. Katoh, N. Yasuda, B. K. Breedlove and M. Yamashita, *Inorg. Chem.*, 2015, **54**, 3297.

[33] D. I. Alexandropoulos, L. Cunha-Silva, L. Pham, V. Bekiari, G. Christou and T. C. Stamatatos, *Inorg. Chem.*, 2014, **53**, 3220.

Table of contents

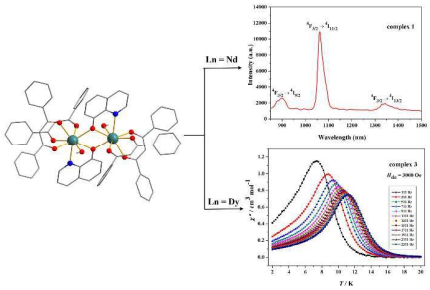

Herein we report near-infrared luminescence properties and SMM behaviors of five new lanthanide complexes based on 8-hydroxyquinoline and dibenzoylmethanate ligands.